

Achieving a Double Advantage Through Design of TiO₂/C Interlaced Coating for Si Anode

Xingwang Shi⁺^[b], Xiangyu Bi⁺^[a], Tianyu Tang⁺^[a], Jiansen Gu,^[b] Yangfan Lu,^[c] Haosheng Jing,^[b] Jiakang Xu,^[b] Jingguo Yang,^[a] Jun Wang,^{*,[b]} Zhiya Zhang,^{*,[a]} and Yong Peng^{*,[d]}

Multifunctional coating strategy shows promising prospective in advancing Si-based anodes towards practical applications in Li-ion batteries. Dual coating of amorphous carbon and TiO₂ shows demonstrable advantages owing to high elasticity of amorphous carbon and mechanical toughness of TiO₂. However, for past design of Si@C@TiO₂ composite electrode, wherein C and TiO₂ are configured layer-by-layer, a long-standing problem exists as that a thin TiO₂ coating is insufficient to stabilize the electrode's architecture while a thick one prevents the core active material of Si far from fully electrochemically utilization due to the too strong structural constraint effect. Herein, it

presents that a facial heat treatment of Si@C@TiO₂ with thick enough TiO₂ can readily avert the problem. Such a strategy promotes the capacity utilization rate from 39% to 61% for the initial cycle and from 43% to 85% after 200 cycles. Model structure of C/TiO₂ multilayer films is employed to reveal the role of the heat treatment. It finds that the heat treatment can transform a layer-by-layer structure of C@TiO₂ into an interlaced structure of C/TiO₂ which exhibits a dual advantage in withstanding mechanical strain and simultaneously promoting Li-ion storage and electron/Li-ion transport.

Introduction

Silicon (Si)-based anode is desired to be used in Li-ion batteries (LIBs) to meet the urgent need for energy storage devices of high energy density, owing to the extraordinary high theoretical specific capacity of Si (3579 mAh g⁻¹, corresponding to Li₁₅Si₄ at room temperature), suitable discharge voltage (~0.34 V vs. Li/Li⁺), natural abundance and environmental benignancy.^[1–5] However, for pure Si anode, the large volume expansion and the formation of highly reactive lithium silicides during the lithiation results in poor electrochemical reversibility and low Coulombic efficiency. In comparison, Si_xO^[6–7] and Si-based core-

shell^[8] structures are more favored for applied LIBs. Additionally, it is hoped that the intrinsically low electron/Li-ion conductivity of Si can be offset by decent structural engineering or compositing with other materials of better electron/Li-ion transport properties.

As for the Si_xO-type anodes, the volumetric effect can be partly alleviated. However, the initial Coulombic efficiency (ICE) is generally low due to the formation of irreversible Li₂O and lithium silicates (e.g., Li₄SiO₄, Li₆Si₂O₇, Li₂SiO₃) in the lithiation process.^[9–15] The strategy of pre-lithiation seems to be the only effective way found so far to solve the low ICE problem.^[16–17] However, it will undoubtedly complicate the battery fabrication procedure, and in addition, it would be practically difficult to accurately control to what level the electrode should be pre-lithiated.

As far as the Si-based core-shell structure concerned, it is becoming a competitive type of Si-based anode. Encapsulating Si with an electronic/ionic conductive shell of high elasticity can release the mechanical strain caused by the huge volumetric change during the de-/lithiation of Si and hence prevents the devastating electrode cracking.^[18–23] Previous researches^[24–26] have demonstrated that the mechanical properties of the shell play a vital role in maintaining the architectural stability of the composite electrode. The shell layer can also protect Si from direct contacting with electrolyte during the cycling process and thus make the electrode more electrochemically stable.

Carbon materials are most commonly used as the buffer matrix for Si. However, previous studies^[27–29] clearly show that the mechanical strength of carbon materials alone is insufficient to mitigate the electrode cracking problem. For constructing a more mechanically strong shell for Si, TiO₂ of a negligible volume variation (<4%) and robust mechanical stability upon de-/lithiation is considered as an ideal candidate.^[30] As expected, core-double-shell composite structures of Si@C@TiO₂

[a] X. Bi,⁺ T. Tang,⁺ J. Yang, Z. Zhang

School of Materials and Energy, Lanzhou University, Lanzhou 730000, China
and

Key Laboratory of Special Function Materials and Structure Design, Ministry of Education, Lanzhou University, Lanzhou 730000, China
E-mail: zhangzhiya@lzu.edu.cn

[b] X. Shi,⁺ J. Gu, H. Jing, J. Xu, J. Wang

School of Materials and Energy, Lanzhou University, Lanzhou 730000, China
E-mail: wangj-phy@lzu.edu.cn

[c] Y. Lu

School of Materials Science and Engineering, Zhejiang University, Hangzhou, 310027, China

[d] Y. Peng

School of Materials and Energy, Lanzhou University, Lanzhou 730000, China
and

Electron Microscopy Centre, Lanzhou University, Lanzhou, 730000, China
E-mail: pengy@lzu.edu.cn

[+] Xingwang Shi, Xiangyu Bi and Tianyu Tang contributed equally. Xingwang Shi prepared the C/TiO₂ multilayer film electrodes and investigated the structural and electrochemical performance. Xiangyu Bi and Tianyu Tang fabricated the Si@C@TiO₂ core-dual-shell electrodes and studied the structural and electrochemical performance.

 Supporting information for this article is available on the WWW under <https://doi.org/10.1002/batt.202400130>

and $\text{Si}@\text{TiO}_2@\text{C}$ exhibit obviously superior electrochemical performance to $\text{Si}@\text{C}$ and $\text{Si}@\text{TiO}_2$. As exemplary work, $\text{Si}@\text{TiO}_2@\text{C}$ hollow nanospheres^[31] showed a discharge capacity of $1270.3 \text{ mAh g}^{-1}$ at a current density of 1000 mA g^{-1} after 250 cycles with an average Coulombic efficiency of 99.53%; void-buffered $\text{Si}@\text{TiO}_2/\text{C}$ microspheres^[32] delivered a reversible capacity of 1038 mAh g^{-1} at a current density of 500 mA g^{-1} after 400 cycles; $\text{Si}/\text{mesoporous-carbon/crystalline-TiO}_2$ nanoparticles^[27] output a capacity of 1010 mAh g^{-1} after 710 cycles at a current density of 420 mA g^{-1} with a Coulombic efficiency over 98%; the structure of micron-sized secondary Si clusters embedded in an amorphous-carbon/ TiO_x matrix conformably formed on the surface of Si^[33] exhibited an initial capacity of 1410 mAh g^{-1} at 100 mA g^{-1} and a capacity retention of ~88% after 200 cycles at 1 A g^{-1} .

Generally, in an integrated core-shell structure, the performance of the core will be limited by the Li-ion storage capacity and electronic/ionic conductivity of the shell. Also, as mentioned above, the mechanical properties of the shell are vital for maintaining the stable architecture of the composite electrode. Commonly, a thicker mechanical binding shell provides better electrode architectural stability; however, the inferior Li-ion storage capability and retarded charge transfer kinetics will slow down the electrochemical reaction and increase the polarization of the electrode. Similar problems are encountered by $\text{Si}@\text{C}@\text{TiO}_2$ composite electrode, specifically, on the mechanical-effect-wise, the layer of TiO_2 should be considerably thick so as to play well the role of volume constraint and structural stabilizer; however, on the wise of electron transport and electrochemical performance, the layer of TiO_2 should be thin enough to avoid deteriorating too much the electrochemical performance of the whole composite electrode, and in addition, too thick TiO_2 and hence over strong volumetric constraint will limit the full de-/lithiation of the active material of Si core. Up to now, there are scarce reports on how to resolve such a conflict, which becomes the first focus of the present work. On the other hand, to experimentally fabricate $\text{Si}@\text{C}@\text{TiO}_2$ or $\text{Si}@\text{TiO}_2@\text{C}$ composite structures, heat treatment is usually necessary to yield a strong interfacial combination between the

heterogeneous shell materials. The heat treatment may result in inter-diffusion or chemical reaction between the heterogeneous shells at and near their interfaces, as suggested in previous studies.^[34–35] The interface state as well as the related effect on the electrochemical properties of the composite electrode is worthy of further exploiting, which is the second focus of the present work.

Herein, we show that the thickness of the TiO_2 layer seriously affects the capacity output of the Si-core in $\text{Si}@\text{C}@\text{TiO}_2$. Through a facial strategy of heat treatment, $\text{Si}@\text{C}@\text{TiO}_2$ containing a thick (~25 nm) TiO_2 shell enables the Si-core to be fully electrochemically reacted. To fundamentally understand the underlying mechanism, we employ C/TiO_2 multilayer films as model structure to reveal the structural evolution upon the heat treatment. We demonstrate that the layer-by-layer structure of C/TiO_2 can be converted into an interlaced structure of C/TiO_2 interweaving with both highly elastic amorphous carbon and stiff TiO_2 under the heat treatment. The interlaced C/TiO_2 composite exhibits a higher Li-ion storage capability and better electronic/ionic conductivity, and simultaneously, a good mechanical strength can be guaranteed by proper TiO_2 thickness and optimal heat treatment condition. Our findings open the way to settle the seeming contradiction between good mechanical stability and good electrochemical performance for TiO_2 -related and TiO_2 -alike coatings for Si-based anodes.

Results and Discussion

Firstly, $\text{Si}@\text{C}@\text{TiO}_2$ core-double-shell structures with different thicknesses of TiO_2 were prepared. The inner shell is characterized as amorphous carbon and the outer shell as TiO_2 of mainly anatase phase. The XRD patterns and Raman shifts of the 8-nm-thick- TiO_2 sample (SCT8) and 25-nm-thick- TiO_2 sample (SCT25) show roughly the same crystalline structure (Figure S1a,b in the supporting information (SI)). The original size of Si powder used in our experiment is ~80 nm. After the coating, the statistic average particle sizes of the SCT8 and SCT25 are ~120 nm and ~160 nm, respectively (Figure S1,d). Figure 1

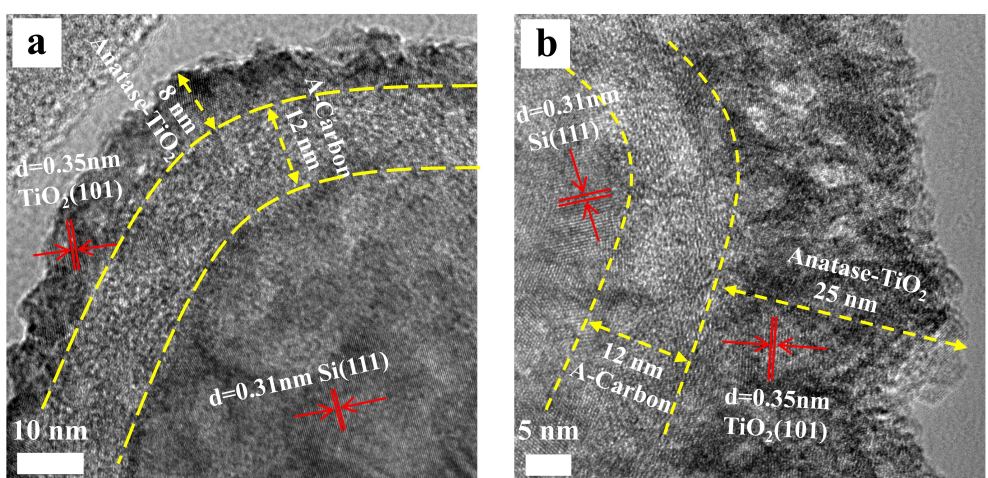


Figure 1. HRTEM images of SCT8 (a) and SCT25 (b).

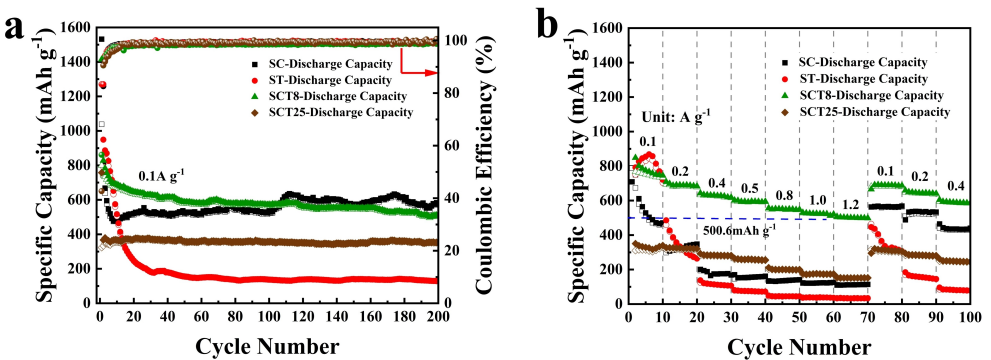


Figure 2. Cycling (a) and rate performance (b) of SC, ST, SCT8 and SCT25 electrodes.

shows the high-resolution TEM (HRTEM) images of the SCT8 and SCT25. It clearly shows the crystalline Si core ((111) plane with 0.31 nm interplanar spacing), amorphous carbon (A-Carbon) inner shell and anatase TiO₂ (Anatase-TiO₂) outer shell ((101) plane with 0.35 nm interplanar spacing). In the SCT8, the thickness of the A-Carbon layer is ~12 nm and that of the Anatase-TiO₂ layer is ~8 nm (Figure 1a). The SCT25 shows almost the same thickness of the A-Carbon layer (~12 nm) and about 25-nm-thick Anatase-TiO₂ layer (Figure 1b). Also, we synthesized Si@C (SC) and Si@TiO₂ (ST) core-shell structures with the same thicknesses of the A-Carbon layer and the Anatase-TiO₂ layer as that of the SCT8 for a contrast study. The corresponding XRD and Raman spectra can be found in Figure S1a,b, and the TEM images in Figure S2.

Figure 2 shows the cycling and rate performance of the SC, ST, SCT8 and SCT25 electrodes. The cycling test is conducted at a charge/discharge current density of 100 mA g⁻¹ with a voltage window of 0.01–3.0 V. Some major data are also listed in Table 1 (the calculation of the theoretical specific capacity of C_T is described in Description S1 in the SI). As can be found, the specific capacity of the ST quickly decays to 130 mAh g⁻¹ after 200 cycles from a high initial capacity of 791 mAh g⁻¹. The SC shows obvious capacity output oscillation upon cycling despite that the capacity is relatively higher. The capacity oscillation has also been previously observed^[36–38] and it was ascribed to the buffering effect of amorphous carbon on the volumetric change of Si, that is, because there was no architectural constraint layer, the electrical contact between the Si@C particles underwent

repeated separation and re-contact due to the repeated volume expansion and contraction during battery cycling. In contrast, the SCT8 exhibits the best overall performance, including the most prominent rate performance (500.6 mAh g⁻¹ at 1.2 A g⁻¹ charge/discharge current density, Figure 2b). The SCT25 outputs a medium and very stable capacity of ~350 mAh g⁻¹. The favored cycling performance of SCT8 and SCT25 can be attributed to the synergistic effect of the double shells of the A-Carbon and Anatase-TiO₂. The “soft” A-Carbon inner shell can buffer the volumetric change of Si and the “hard” Anatase-TiO₂ outer shell can stabilize the whole architecture. The difference in cycling stability of the SCT8 and SCT25 is correlated with the weak and strong binding effect from the thin and thick Anatase-TiO₂, respectively. With a thick shell of 25-nm-thick-TiO₂, the SCT25 shows particularly high cycling stability, it however outputs a plain specific capacity (~350 mAh g⁻¹). This can be easily understood that the 25-nm-thick-TiO₂ is too thick and holds up the Li-ion transport into the Si core. In our experiment, it is interestingly found that with a facile heat treatment of SCT25, the corresponding electrode (SCT25L) outperforms both the SCT8 and SCT25, which will be discussed later.

The cyclic voltammetry (CV) curves and electrochemical impedance spectroscopy (EIS) of the SC, ST, SCT8, SCT25 and SCT25L electrodes are shown in Figure 3. For the former four electrodes, the redox peaks of Si(C) (<1.0 V) and anatase TiO₂ (>1.5 V) can be resolved from the CV curves, as shown in Figure 3a1–a4. The situation is peculiar for the SCT25L, for which the CV peaks of TiO₂ are obscured. This result suggests that TiO₂ in the shell may transform into refined TiO₂ domains under the heat treatment. Previous studies^[39–41] have shown that the phase diagram of TiO₂ upon de-/lithiation is strongly size dependent, and with decreasing the particle size, the two-phase (Li-rich phase and Li-poor phase) de-/lithiation mechanism will be altered to solid solution reaction behavior. Accordingly, the charge/discharge plateau corresponding to the two-phase reaction will change to be a tilt line corresponding to the solid-solution reaction, and consequently, the CV peaks will be smeared in the CV curves. The result is also consistent with that revealed by the study on model structure of C/TiO₂ multilayer films in later discussions, wherein, C/TiO₂ interlaced structure and nano domains of TiO₂ are demonstrated to be

Table 1. Initial discharge/charge specific capacities (IDC/ICC), specific capacities after 200 cycles (C_E), theoretic specific capacities (C_T) and the percentage ratio of ICC to C_T (ICC/C_T) and C_E to C_T (C_E/C_T) of SC, ST, SCT8, SCT25 and SCT25L electrodes.

Electrodes	IDC/ICC (mAh g ⁻¹)	ICC/C _T (%)	C _E (mAh g ⁻¹)	C _T (mAh g ⁻¹)	C _E /C _T (%)
SC	1532/1038	61	583	1690	35
ST	949/791	31	130	2557	5
SCT8	1415/799	54	505	1476	34
SCT25	758/323	39	353	830	43
SCT25L	798/505	61	707	830	85

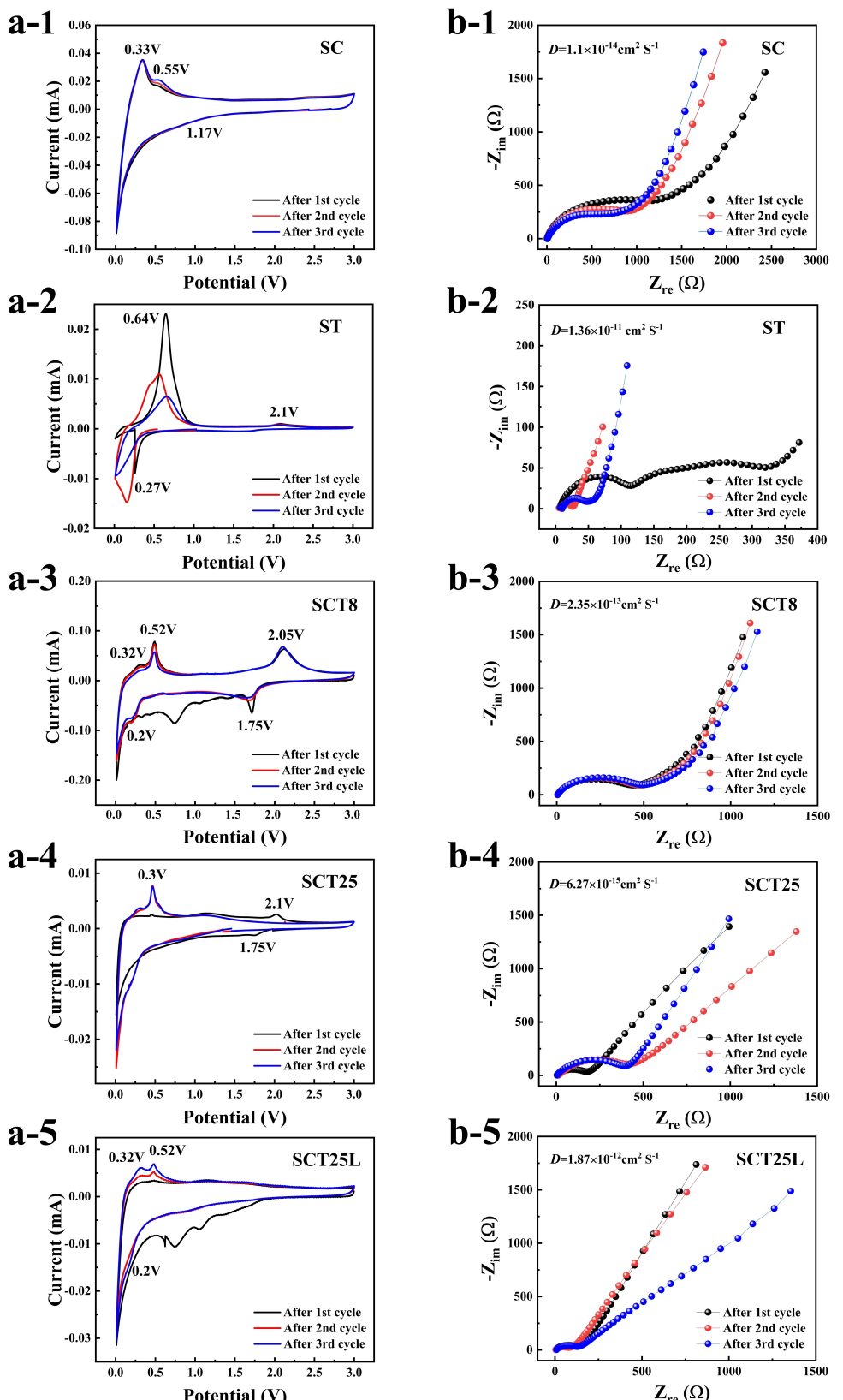


Figure 3. CV curves (a) and EISs (b) of SC (1), ST (2), SCT8 (3), SCT25 (4) and SCT25L (5) electrodes.

produced under heat treatment. It should be for the same reason, the charge transfer resistance (R_{ct} , represented by the

depressed semicircle diameter of the EIS in Figure 3b) of the SCT25L is decreased significantly as compared to those of the

SCT8 and SCT25. It is worthy of mentioning that the SC electrode has the largest R_{ct} and the ST electrode the smallest R_{ct} , reflecting faster electrochemical reaction kinetics of carbon than of anatase-TiO₂.

The evaluated apparent Li-ion diffusion coefficients (D) of the electrodes are indicated in Figure 3. The evaluation is applied based on the dependence of the real part of electrode impedance (Z_{re}) on the reciprocal of square root of angular frequency ($\omega^{-1/2}$) in the low frequency region of (see Figure S4 and Description S2 for details). It can be found that the thickness of the TiO₂ layer seriously affects the Li-ion diffusion dynamics and from the SCT8 to SCT25 the D decreases from $2.35 \times 10^{-13} \text{ cm}^2 \text{ s}^{-1}$ to $6.27 \times 10^{-15} \text{ cm}^2 \text{ s}^{-1}$. However, after the SCT25 is heat treated, the as-obtained SCT25L achieves a significantly improved Li-ion diffusion kinetics and the D is promoted from $6.27 \times 10^{-15} \text{ cm}^2 \text{ s}^{-1}$ to $1.87 \times 10^{-12} \text{ cm}^2 \text{ s}^{-1}$. These results elucidate the importance of structural modulation of the coating layer in finally obtaining a satisfactory electrochemical performance of Si-based composite electrode.

The SEM images of the SCT8 and SCT25 electrodes after 200 cycles are shown in Figure S5a,b. There appear severe cracks in the SCT8 electrode whereas the SCT25 electrode remains fairly intact. The results explicitly show that, although the SCT8 has potential Li-ion storage capability and excellent rate performance, the strength of the thin TiO₂ shell is not enough to bind and stabilize the electrode architecture; in contrast, the thick

TiO₂ shell stabilizes well the SCT25 electrode but holds up the Li-ion transport to the core, resulting in inferior electrochemical performance.

Interestingly, our experiment finds that a further heat treatment of SCT25 at 500 °C for 3 h (the corresponding sample is denoted as SCT25L) can successfully avert the above problem in the SCT25. After the heat treatment, there is a small amount of rutile TiO₂ newly appeared (Figure S1a) and the SEM morphology shows no apparent difference (Figure S1d,e). Figure 4a is a comparison of cycling performance of the SCT8, SCT25 and SCT25L. The related data is also shown in Table 1. As can be found, the SCT25L exhibits the most superior capacity release, *i.e.*, the ratio of the experimental specific capacity relative to the theoretical specific capacity, and comparable rate performance (Figure S6), as compared with the SCT8 and SCT25. Even though with a relatively lower theoretical specific capacity, the SCT25L greatly outperforms all the other electrodes after 200 cycles, delivering a specific capacity as high as 707 mAh g⁻¹. The corresponding capacity utilization rate (*i.e.*, C_e/C_t) is evaluated to be 85% (Table 1), which is found to be relatively higher than those of reported Si-C composites as illustrated in Table S1.

The SEM image of the SCT25L electrode after 200 cycles (Figure S5c) shows only a slight cracking, which is in a sharp contrast to the case of the SCT8 that shows severe electrode fracture (Figure S5a). Also as shown in the HRTEM images of the

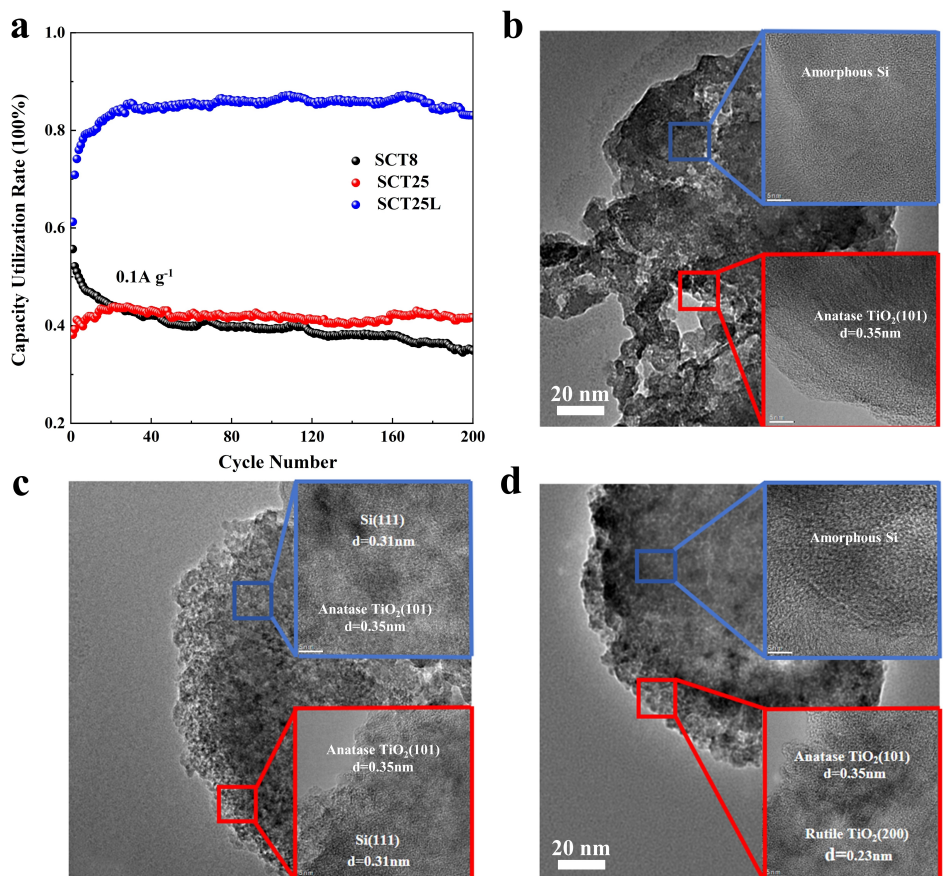


Figure 4. Capacity utilization rates (a) and HRTEM images of SCT8 (b), SCT25 (c) and SCT25L (d) electrodes after 200 cycles.

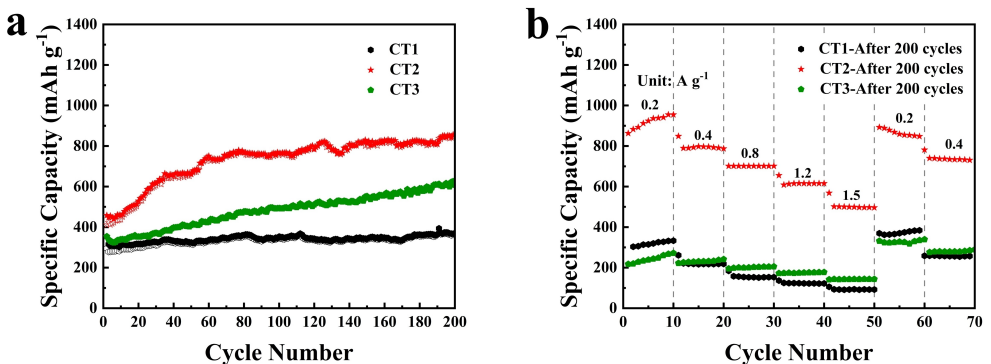


Figure 5. Cycling (a) and rate performance after 200 cycles (b) of CT1-CT3 electrodes.

electrodes after 200 cycles (Figure 4b-d), the shells of both the SCT25 and SCT25L remain intact; in contrast, the shell of the SCT8 is substantially destroyed, which explains the lower capacity utilization of SCT8 considering the electrical contact lost. It should be mentioned that the electrode cracking as well as the damage of the coating layer may lead to a superficial promotion of rate performance as in the case of the SCT8. It is additionally found that the Si-core in the SCT25L is mainly amorphous (Figure 4d) while it is mainly crystalline in the SCT25 (Figure 4c), further verifying the superior capacity utilization in the SCT25L (Figure 4a and Table 1).

To understand how the C@TiO₂ double shell of the SCT25 changed with the heat treatment, a chemical composition analysis across the C/TiO₂ heterointerface is necessary. However, it is difficult to realize such analysis reliably and feasibly using conventional techniques such as X-ray photoelectron spectroscopy (XPS) and HRTEM in nanoparticle materials. Multilayer film structure is just convenient for such investigations^[1,42] and will be employed as model structure here. Multilayer film structure has multiple parallel macro-size area of heterointerfaces and the cross section chemical composition analysis can be easily conducted with the help of ion etching; it also facilitates the study of the interfacial effect on the electrochemical properties considering the multiple parallel heterointerfaces can greatly magnify the interfacial reactions.

Accordingly, C/TiO₂ multilayer films structures are employed to reveal how the thickness of TiO₂ and the heat treatment influence the electrochemical response of the C/TiO₂ heterostructure. Amorphous-carbon/amorphous-TiO₂ multilayer films are firstly deposited, and then are heat treated at 500 °C for 2 h in an Ar atmosphere to obtain amorphous-carbon/anatase-TiO₂ multilayer films. The periodic thickness of the carbon layer is fixed to 12 nm, and that of the TiO₂ layer is designed as 6, 10 and 15 nm, respectively. The corresponding samples are denoted as CT1, CT2 and CT3.

As displayed in Figure 5 and Table 2, the CT2 presents the best cycling and rate performance. It outputs the highest specific capacity after 200 cycles (~900 mAh g⁻¹). It should be noted that the theoretical capacity of C_T as listed in Table 2 is calculated by using the specific capacities of amorphous carbon and anatase TiO₂ with the weighted average method and does not include the effect of C/TiO₂ interfaces, and so that the

Table 2. Specific capacities after 200 cycles (C_E), theoretical specific capacities (C_T) and the ratio of the C_E to C_T (C_E/C_T) for CT1-CT3 electrodes.

Electrodes	C _E (mAh g ⁻¹)	C _T (mAh g ⁻¹)	C _E /C _T (%)
CT1	363	243	149
CT2	900	229	393
CT3	578	219	264

surplus of the experimental value of C_E relative to the C_T can be a good index of the C/TiO₂ interfacial effect. The CT2 exhibits the highest C_E/C_T (~400 %), suggesting that the CT2 has the largest amount of C/TiO₂ interfaces. In addition, it can be found that the specific capacity of the CT2 after 200 cycles is nearly doubled as compared to the initial specific capacity, and those of CT1 and CT3 are also increased in different degrees (Figure 5a). Similar phenomenon has also been observed in Si/TiO₂ multilayer film anodes^[43] and Si@SiO_x core-shell anodes.^[44] It might be correlated with the continuous microstructure evolution such as particle size reduction as the reaction proceeds. However, direct evidence requires future studies using techniques such as *in-situ* TEM.

Figure 6a,b show the cross-sectional HRTEM images of the CT2. The texture of TiO₂ (dark) and carbon (bright) can be clearly seen. In some locations, the carbon layer becomes too narrow and the two originally separated TiO₂ appears connected. The TiO₂ domain is dominated by anatase with a small amount of rutile phase. The XRD and Raman spectra of the CT1-CT3 are shown in Figure S7. Figure 6c shows the cross-sectional elemental distributions of C, Ti and O in the CT2. As can be found, the periodicity of the elemental distributions almost disappears, demonstrating that the film is not of a layer-by-layer structure of C@TiO₂ anymore but of an intertwined composite structure of C/TiO₂. It indicates that effective inter-diffusion between C and TiO₂ occurred during the heat treatment. The formation mechanism of the C/TiO₂ interlaced composite structure is tentatively proposed here: under heat treating, the TiO₂ component gradually crystallizes and the carbon atoms migrates and penetrates into the TiO₂ grain boundaries, which on the one hand successfully prevents the TiO₂ crystalline grains from continuous growing, and on the other hand, creates new abundant C/TiO₂ interfaces. Combining the electrochemical

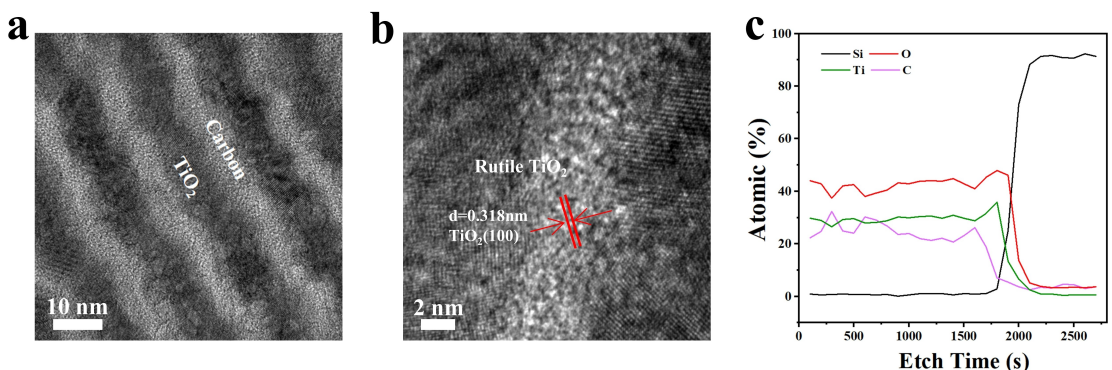


Figure 6. Cross-sectional HRTEM images (a, b) and elemental distributions of C, Ti and O (c) of CT2.

properties discussed above (Figure 5 and Table 2), it shows that an appropriate thickness ratio of carbon layer to TiO₂ layer in the as-deposited film creates an optimum amount of C/TiO₂ interfaces after heat treating as in the case of the CT2. It has been noticed that a similar coating strategy was recently proposed.^[45] The authors firstly coated Si nanoparticles with a polymerized substance containing Si and C and then annealed the coated structure at 800 °C. An interfused coating layer of SiO_x/C was finally formed on Si particles and it presented both superior mechanical and electrochemical properties.

Considering relatively higher Li-ion diffusivity of rutile TiO₂ ($10^{-6} \text{ cm}^2 \text{s}^{-1}$ along *c* axis and $10^{-15} \text{ cm}^2 \text{s}^{-1}$ along *a* axis) than anatase TiO₂ ($10^{-11} \text{ cm}^2 \text{s}^{-1}$)^[41] the newly

formed rutile TiO₂ upon the heat treatment should be favorable for improving the electrochemical performance of the composite electrode. However, that might not be true actually. As recently reported,^[46] below 1.2 V, rutile TiO₂ undergoes an irreversible phase transformation into disordered rock salt-type c-LiT₂O₂, in which lithium diffusion is actually very low (10^{-16} – $10^{-15} \text{ cm}^2 \text{s}^{-1}$) and most capacity arises from capacitive processes. Indeed, in the C/TiO₂ interlaced structure, the abundant C/TiO₂ interface in fact plays a prominent role in deciding the electrochemical performance, as discussed later.

Figure 7 shows the high-resolution XPS of the CT2 (with 2 h heat treatment) and the corresponding as-deposited film of a-CT2 (without heat treatment). As indicated from Figure 7a,b, in the a-CT2 carbon exists as sp² (284.5 eV) and sp³ (285.0 eV) of diamond-like carbon^[47] and titanium appears as Ti⁴⁺ (456.6 eV) and Ti³⁺ (457.9 eV).^[48–49] In contrast, in the CT2 (Figure 7c,d) carbon exists as sp² (284.1 eV) of graphene/graphite-like carbon,^[50–53] and sp² (284.5 eV) and sp³ (285.0 eV) of diamond-like carbon. The emergence of graphene/graphite-like carbon atoms connection is further verified by the appearance of the G' peak^[54–55] around 2700 cm⁻¹ in the Raman spectra (Figure S7b), demonstrating that carbon is locally ordered after the heat treatment. The graphitized carbon will be beneficial for the electrical conductivity of the composite structure. A comparison of the Raman spectra of the CT1-CT3 with that of the a-CT2 (Figure S7b) also explicitly shows that after the heat treatment crystalline TiO₂ are generated. As indicated in Figure 7d, titanium in the CT2 exists in three forms of Ti⁴⁺, Ti³⁺ and Ti²⁺. The presence of Ti³⁺ species in TiO₂ usually means an

concurrence of oxygen vacancies^[56–57] and such crystalline defects can promote the electrical conductivity and provide further Li-ion storage sites. The Ti²⁺ species represent a trap state and mainly come from the surface of TiO₂ grains and it is believed to be a major feature of nano-sized TiO₂.^[58–59] The prominent Ti²⁺ signal in the CT2 (Figure 7d,f) suggests that nano grains of TiO₂ are formed. The Ti²⁺ species can also increase the electrical conductivity of TiO₂.^[59–60] As displayed in Figure 7e,f, the signals of C 1s and Ti 2p are both depth independent, demonstrating that a C/TiO₂ interpenetrating structure has been formed.

The above discussion demonstrates three important changes that take place after the as-deposited C/TiO₂ multilayer films are heat treated: (1) carbon are locally graphitized, (2) Ti³⁺ and Ti²⁺ are generated across the C/TiO₂ interfaces, and (3) abundant C/TiO₂ interfaces are created. These aspects jointly would make the surface-related electrochemical process prominent. By analyzing the CV data according to $i = av^b$ ^[61] and separating the surface capacitive effect from the diffusion-controlled insertion process based on $i(V) = k_1v + k_2v^{1/2}$ ^[62] at various sweep rates, it is found that the Li-ion storage of the CT1-CT3 is truly dominated by surface capacitive effect, as indicated in Figure S11 and Figure S12. Previous reports^[63–67] suggest a similar mechanism that C/TiO₂ nanocomposites yield prominent pseudocapacitive capacity.

As reported,^[39–41] the de-/lithiation of nano-sized TiO₂ was different from its bulk counterpart. Upon Li-ion insertion, it underwent a reversible crystalline-amorphous phase transformation rather than a Li_{0.5}TiO₂–LiTiO₂ core-shell configuration. The amorphous phase as formed could facilitate fast Li-ion diffusion, and the amorphous reaction path made a lift of the kinetic limitation imposed by the Li_{0.5}TiO₂–LiTiO₂ mechanism that is typical for bulk anatase and consequently nearly full lithiation (Li_xTiO₂, $x \rightarrow 1.0$) could be achieved. The similar mechanism may take function here in the C/TiO₂ interlaced structure. In addition, at the heterogeneous interface of C/TiO₂, a built-in electric field can be formed due to their band alignment. The built-in electric field may improve the capacitive capacity and increase the Li-ion transport kinetics and rate performance.

The typical CV curves (Figure 8a) present a pair of redox peaks located at A and B as marked. They can be attributed

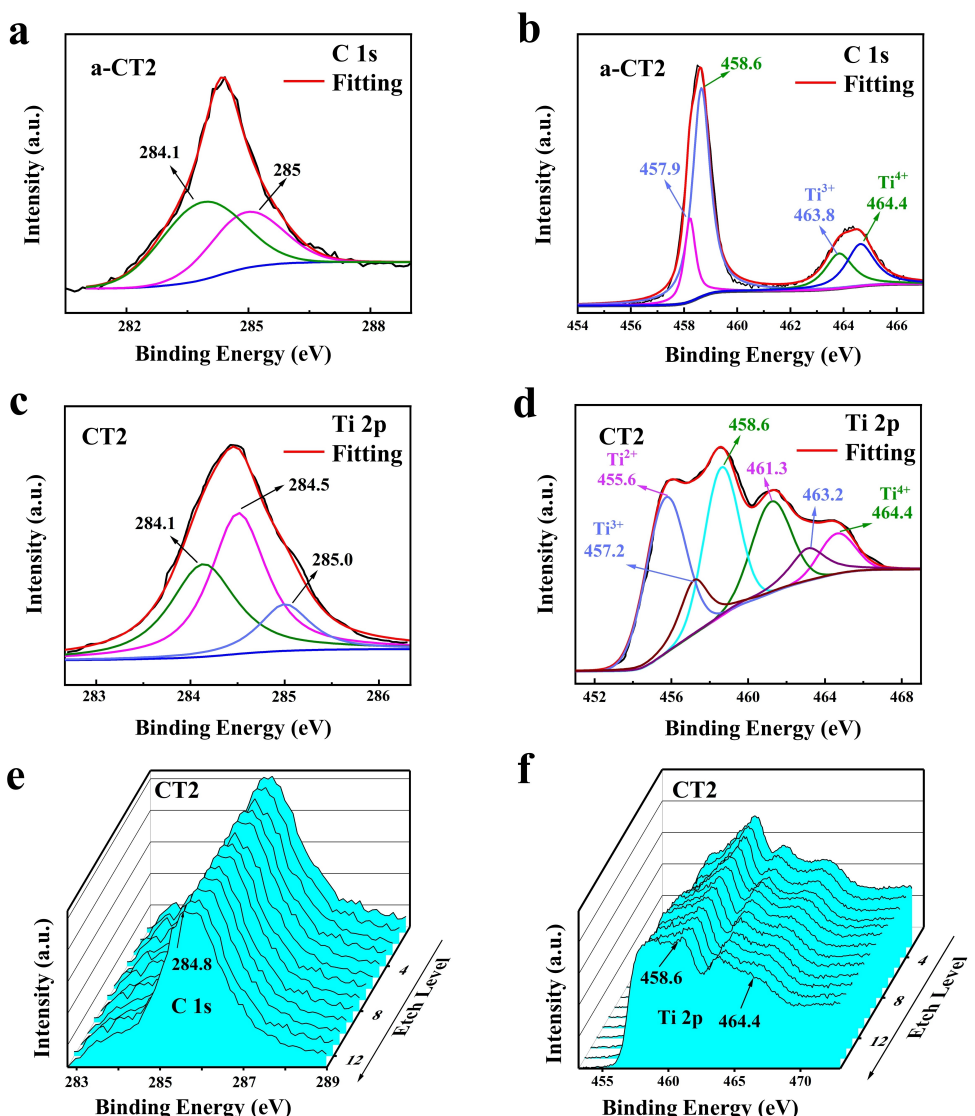


Figure 7. Gauss fittings of high-resolution XPS of C 1s and Ti 2p of a-CT2 ((a), (b)) and CT2 ((c), (d)). High-resolution XPS of C 1s (e) and Ti 2p (f) of CT2.

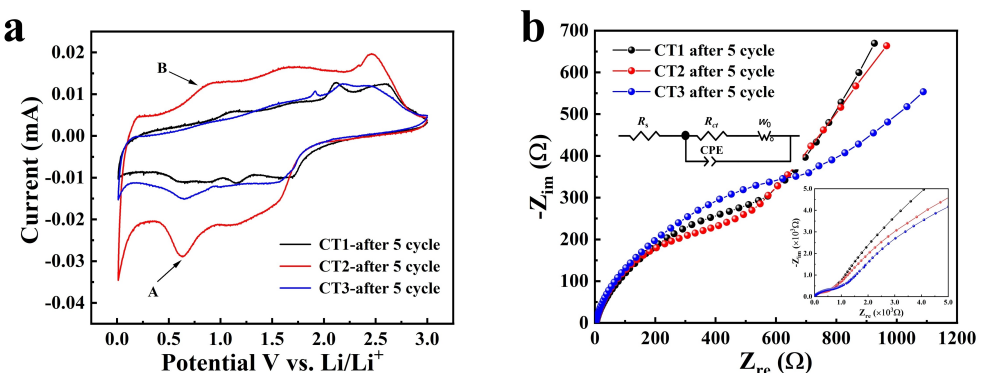


Figure 8. CV curves (a) and EISs (b) of CT1-CT3 electrodes after 5 cycles.

to the electrochemical reactions related to the C/TiO₂ composite since they cannot be explicitly assigned to the contributions of both C and TiO₂. As can be seen, the CT2 has the strongest A and B peaks, manifesting the optimal interwoven structure of

carbon with TiO₂. The other CV curves are given in Figure S8 and the charge/discharge curves in Figure S9a–c.

The EISs of the CT1-CT3 are shown in Figure 8b (inset shows the equivalent circuit). The fitting results as well as the

evaluated D are listed in Table 3. As can be found, the CT2 has the smallest R_{ct} among the three electrodes. The D of the three electrodes is comparable and that of the CT2 is slightly higher. However, they are apparently higher than amorphous carbon and anatase-TiO₂ film electrodes.^[64,68]

Further, the mechanical properties of the CT1-CT3 are characterized by a nanoindentation measurement, as shown in Figure 9. The results show that as the amount of the TiO₂ component increases from the CT1 to CT3, the hardness and elastic modulus of the C/TiO₂ composite film increase accordingly. However, as the CT3 which shows the best mechanical property is further heat treated for 2 h (the corresponding sample is denoted as CT3'), the hardness and elastic modulus decreases. Therefore, in order to ensure that the C/TiO₂ has sufficient mechanical strength, a thick enough TiO₂ layer should be used and the heat treatment condition should be optimized.

As control experiment, the CT4, CT5 and CT6 with the same composition ratio as that of the CT1, CT2 and CT3, respectively, were prepared by co-sputtering carbon and TiO₂. It is found that the CT5 that has the same composition ratio as the CT2 exhibits the highest specific capacity (Figure S13). The cycling stability of the CT4-CT6 is significantly better than the CT1-CT3 (Figure 5 and Figure S13). The structural (Figure S7 and Figure S14) and other electrochemical properties (Figures S8d-f, S9d-f, S11d-f, S12d-f and S15, Tables S2 and S3) are not intrinsically different from those of the CT1-CT3.

Conclusions

We presented that in the composite anode of core-double-shell Si@C@TiO₂, the thickness of TiO₂ influenced the electrode performance in a seeming contradicting way: a thick TiO₂ coating (~25 nm) supported for a good mechanical stability but deteriorated the utilization of the coated active material of Si core. We have demonstrated that a facial heat treatment of the Si@C@TiO₂ could dismiss the above problem. By employing and studying model structure of C/TiO₂ multilayer films, it was proposed that upon the heat treatment, the layer-by-layer coating of C@TiO₂ in the Si@C@TiO₂ could be transformed to an interlaced coating of C/TiO₂. In addition, the other structural changes observed in the model structures, *i.e.*, locally graphitized carbon, Ti³⁺ and Ti²⁺ created across the C/TiO₂ interfaces, the formed nano-sized TiO₂ domains, and the created abundant C/TiO₂ interfaces beneficial to promote the electrode's electrochemical performances were believed to occur similarly in the Si@C@TiO₂. These results highlight the importance of structural modulation of the coating layer(s) in actually gaining a superior electrochemical performance of Si-based composite electrodes.

Experimental Section

Materials Synthesis

Preparation of the Powder Materials (SC, ST, SCT8, SCT25 and SCT25L)

The Si@C core-shell nanocomposites (SC) were prepared by coating a layer of dopamine on the surface of silicon nanoparticles and carbonizing the dopamine by a subsequent heat treatment. 0.1 g of silicon nanospheres was dispersed in 50 mL Tris-buffer (0.01 M, pH = 8.5) to form a suspension. Subsequently 50 mg of dopamine was added to the suspension and stirred continuously for 24 h. The precipitate was collected, washed repeatedly with deionized water and then dried in vacuum. The obtained powders were heat treated at 800°C for 3 h with a heating rate of 5 °C min⁻¹ in an Ar atmosphere.

Si@TiO₂ core-shell nanocomposites (ST) were synthesized using a sol-gel method. First, 1 g of hydroxypropyl cellulose (HPC, molecular weight: 100,000, Aldrich) was dissolved in 400 mL of ethanol. Then, 0.2 g of the silicon nanospheres and 4 mL of deionized water

Table 3. EIS fitting results (R_{ct} : charge transfer resistance) and the calculated apparent Li-ion diffusion coefficients (D) of amorphous carbon film electrode (C), anatase-TiO₂ film electrode (TiO₂) and CT1-CT3 electrodes after 5 cycles.

Electrodes	R_{ct} (Ω)	D (cm ² s ⁻¹)
C	628	3.42×10^{-15}
TiO ₂	467	2.13×10^{-16}
CT1	586	2.63×10^{-14}
CT2	535	3.46×10^{-14}
CT3	694	2.04×10^{-14}

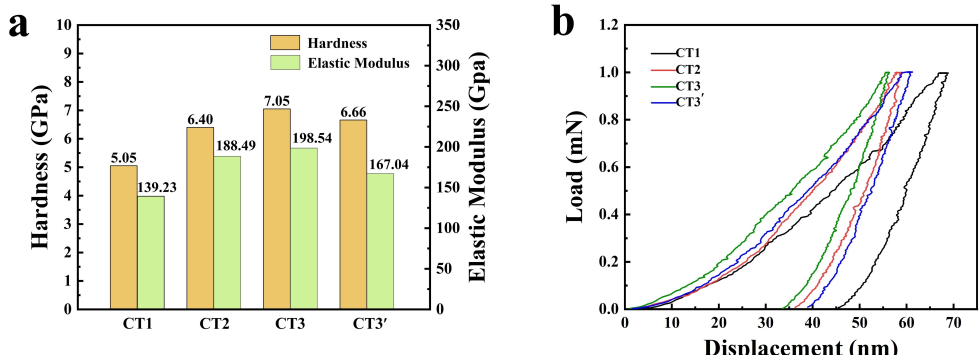


Figure 9. Hardness and elastic modulus (a) derived from the displacement-load curves measured by a nanoindentation method (b) of CT1-CT3 and CT3'.

were added. Subsequently, 1 g of titanium butoxide (TBOT, $\text{Ti}(\text{OC}_4\text{H}_9)_4$, 97%, Aldrich) solution dissolved in 40 ml of ethanol was added dropwise to the above solution and stirred at 90 °C for 3 h. The resulting product was washed, collected and dried in a vacuum oven at 90 °C for 12 h. The obtained powders were then heat treated at 500 °C for 3 h with a heating rate of 5 °C min⁻¹ in an Ar atmosphere.

The Si@C@TiO₂ core-double-shell nanocomposites (SCT) were synthesized by the similar sol-gel method preparing the ST. By replacing the Si nanoparticles with the Si@C nanoparticles prepared in the above experiments, Si@C@TiO₂ of SCT8 was obtained. Following the above experimental protocol and changing the amount of titanium butoxide solution to 6 g, Si@C@TiO₂ of SCT25 was obtained. By further heat treating SCT25 in an Ar atmosphere at 500 °C for 3 h, SCT25L was obtained.

Preparation of C/TiO₂ Multilayer Films (CT1-CT6)

The C/TiO₂ films (CT1-CT6) with Ti(C) transition layer were prepared via a pulsed direct current (DC) magnetron sputtering method using *n*-type amorphous C (purity 99.999%), amorphous TiO₂ (purity 99.95%) and titanium (purity 99.995 %) as the targets. The copper foil was polished rough and fixed to the substrate of single crystal silicon wafer. The substrate was evacuated to a pressure below 3×10^{-4} Pa, and the working pressure was controlled to 1.0 Pa by introducing Ar gas (20 sccm) before starting the sputtering. Prior to the preparation of the C/TiO₂ film, a 25-nm-thick Ti(C) transition layer was deposited on the copper foil to improve the adhesion between the active material and the collector. Two sets of samples of CT1-CT3 and CT4-CT6 were prepared. The former were prepared by depositing C targets and TiO₂ targets on the substrate in alternating layers, while the latter were obtained by co-sputtering the C targets and TiO₂ targets. The total thickness of all the samples was controlled as around 360 nm. The as-deposited samples were finally heat treated at 500 °C for 2 h under an Ar atmosphere to obtain the amorphous-carbon/anatase-TiO₂ films of CT1-CT6.

Structural Characterization

The morphology and microstructure of the samples were characterized by Apreo S scanning electron microscope (SEM) and Tecani F30 transmission electron microscope (TEM). The particle size statistics were executed by using Nano Measurer software based on the SEM measurements. The crystal structure of the samples was characterized by powder X-ray diffraction (XRD) using a Cu K α ($\lambda = 1.54056$ Å) X-ray source on Philip X'Pert pro diffractometer. The Raman spectra were recorded at room temperature with a 532 nm YAG laser on HORIBA Jobin Yvon LabRAM HR800. The chemical environment of Ti, N and O elements is characterized by X-ray photoelectron spectroscopy (XPS, Kartos AXIS Ultra DLD) that utilizes a monochromatic Al K α X-ray source ($h\nu = 1486.6$ eV).

Electrochemical Measurements

For the powder samples, the corresponding electrodes were prepared according to the following steps. The powder material as the active substance (70 wt.%) was mixed well with acetylene black (20 wt.%) conductive agent, and then a bonding agent (polyimide (PAI, 10 wt.%) in N-methyl-pyrrolidone) was added dropwise. The obtained slurry was coated onto polished copper foil and dried in a vacuum oven at 90 °C for 12 h. For the prepared thin films, they were directly used as anode without adding binders and conductive agents. The 2032-coin-type half-cells were assembled in an Ar-filled glove box ($[\text{O}_2] < 0.01$ ppm, $[\text{H}_2\text{O}] < 0.01$ ppm), using pure

lithium foil as the counter electrode. A microporous membrane was used as the separator. The used electrolyte was 1 M LiPF₆ dissolved in a solvent of EC/DEC (1:1). The assembled half-cells were electrostatically cycled on a Land CT2001 A system over a voltage range of 0.01–3.0 V vs. Li/Li⁺. The cyclic voltammetry (CV) was tested on a AUTOLAB PGSTAT302 N (Metrohm, Netherlands) electrochemical workstation in a voltage range of 0.01–3.0 V. The electrochemical impedance spectroscopy (EIS) was recorded on the same electrochemical workstation in the frequency range from 10^{-2} to 10^6 Hz with an alternating amplitude of 5 mV.

Acknowledgements

This work was supported by the National Natural Science Foundation of China (12374011 and 51771085) and National Key Research and Development Program of China (2022YFC2903504).

Conflict of Interests

The authors have no financial/commercial conflicts of interest.

Data Availability Statement

Research data are not shared.

Keywords: Si@C/TiO₂ composite anode • multifunctional coating • C/TiO₂ interlaced coating

- [1] Y. Zhao, J. Wang, Q. He, J. Shi, Z. Zhang, X. Men, D. Yan, H. Wang, *ACS Nano* **2019**, *13*, 5602, doi: 10.1021/acsnano.9b00670.
- [2] D. Vrankovic, M. Graczyk-Zajac, C. Kalcher, J. Rohrer, M. Becker, C. Stabler, G. Trykowski, K. Albe, R. Riedel, *ACS Nano* **2017**, *11*, 11409, doi: 10.1021/acsnano.7b06031.
- [3] T. Song, J. Xia, J.-H. Lee, D. H. Lee, M.-S. Kwon, J.-M. Choi, J. Wu, S. K. Doo, H. Chang, W. I. Park, D. S. Zang, H. Kim, Y. Huang, K.-C. Hwang, J. A. Rogers, U. Paik, *Nano Lett.* **2010**, *10*, 1710, doi: 10.1021/nl100086e.
- [4] K. Ababtain, G. Babu, S. Susarla, H. Gullapalli, N. Masurkar, P. M. Ajayan, L. M. R. Arava, *Mater. Res. Express* **2018**, *5*, 2053, doi: 10.1088/2053-1591/aaa0f9.
- [5] L. Zhang, R. Rajagopalan, H. Guo, X. Hu, S. Dou, H. Liu, *Adv. Funct. Mater.* **2016**, *26*, 440, doi: 10.1002/adfm.201503777.
- [6] Y.-S. Choi, D. O. Scanlon, J.-C. Lee, *Adv. Energy Mater.* **2020**, *11*, 2003078, doi: 10.1002/aenm.202003078.
- [7] H. Wu, M. Wang, W. Wu, D. Bai, Y. Liang, S. Hu, W. Yu, P. He, J. Zhang, *J. Mater. Chem. A* **2023**, *11*, 9626, doi: 10.1039/d2ta08226h.
- [8] S. Gunasekaran, D. Thangaraju, R. Marnadu, J. Chandrasekaran, T. Alshahrani, M. Shkir, A. Durairajan, M. P. F. Graça, M. Elango, *Sur. Interfaces* **2020**, *20*, 100622, doi: 10.1016/j.surfin.2020.100622.
- [9] C. Guo, D. Wang, T. Liu, J. Zhu, X. Lang, *J. Mater. Chem. A* **2014**, *2*, 3521, doi: 10.1039/C3TA13746E.
- [10] S. Guo, H. Li, Y. Li, Y. Han, K. Chen, G. Xu, Y. Zhu, X. Hu, *Adv. Energy Mater.* **2018**, *8*, 1800434, doi: 10.1002/aenm.201800434.
- [11] B. Jiang, S. Zeng, H. Wang, D. Liu, J. Qian, Y. Cao, H. Yang, X. Ai, *ACS Appl. Mater. Interfaces* **2016**, *8*, 31611, doi: 10.1021/acsami.6b09775.
- [12] S.-K. Lee, S.-M. Oh, E. Park, B. Scrosati, J. Hassoun, M.-S. Park, Y.-J. Kim, H. Kim, I. Belharouak, Y.-K. Sun, *Nano Lett.* **2015**, *15*, 2863, doi: 10.1021/nl504460s.
- [13] J. Lee, J. Moon, S. A. Han, J. Kim, V. Malgras, Y.-U. Heo, H. Kim, S.-M. Lee, H. K. Liu, S. X. Dou, Y. Yamauchi, M.-S. Park, J. H. Kim, *ACS Nano* **2019**, *13*, 9607, doi: 10.1021/acsnano.9b04725.

- [14] X. Zhuang, P. Song, G. Chen, L. Shi, Y. Wu, X. Tao, H. Liu, D. Zhang, *ACS Appl. Mater. Interfaces* **2017**, *9*, 28464, doi: 10.1021/acsmami.7b05255.
- [15] K. Kitada, O. Pecher, P. M. Magusin, M. F. Groh, R. S. Weatherup, C. P. Grey, *J. Am. Chem. Soc.* **2019**, *141*, 7014, doi: 10.1021/jacs.9b01589.
- [16] B. Huang, T. Huang, L. Wan, A. Yu, *ACS Sustainable Chem. Eng.* **2021**, *9*, 648, doi: 10.1021/acsschemeng.1c05162.
- [17] X. Zhang, H. Ou, W. Ji, D. Zheng, T. Ding, D. Qiu, D. Qu, *J. Power Sources* **2020**, *478*, 229067, doi: 10.1016/j.jpowsour.2020.229067.
- [18] B.-S. Lee, S.-B. Son, K.-M. Park, J.-H. Seo, S.-H. Lee, I.-S. Choi, K.-H. Oh, W.-R. Yu, *J. Power Sources* **2012**, *206*, 267, doi: 10.1016/j.jpowsour.2012.01.120.
- [19] N. Nekić, J. Sancho-Parramon, I. Bogdanović-Radović, J. Grenzer, R. Hübner, S. Bernstorff, M. Ivanda, M. Buljan, *Nat. Photonics* **2017**, *6*, 1055, doi: 10.1511/nanoph-2016-0133.
- [20] I. G. Aykac, O. Ozdemir, C. Taner, L. C. Arslan, *J. Supercond. Novel Magn.* **2020**, *33*, 3929, doi: 10.1007/s10948-020-05600-4.
- [21] K. Wang, N. Li, J. Xie, G. Lei, C. Song, S. Wang, P. Dai, X. Liu, J. Zhang, X. Guo, *Electrochim. Acta* **2021**, *372*, 137863, doi: 10.1016/j.electacta.2021.137863.
- [22] W. Zhang, J. Li, P. Guan, C. Lv, C. Yang, N. Han, X. Wang, G. Song, Z. Peng, *J. Alloys Compd.* **2020**, *835*, 155135, doi: 10.1016/j.jallcom.2020.155135.
- [23] S. Guo, X. Hu, Y. Hou, Z. Wen, *ACS Appl. Mater. Interfaces* **2017**, *9*, 42084, doi: 10.1021/acsmami.7b13035.
- [24] S. Li, D. A. Matos-Fernandez, M. O. Cruz, *ACS Nano* **2021**, *15*, 14804, doi: 10.1021/acsnano.1c04795.
- [25] X. Chu, J. Tang, Z. Geng, X. Wang, G. Huo, L. Zhou, J. Wang, K. Yuan, X. Yang, J. Hu, F. Yang, X. Zhou, L. Zhang, *Langmuir* **2019**, *35*, 17090, doi: 10.1021/acs.langmuir.9b02930.
- [26] J. Sahari, M. A. Maleque, *Int. J. Polym. Sci.* **2016**, *2016*, 7457506, doi: 10.1155/2016/7457506.
- [27] W. Luo, Y. Wang, L. Wang, W. Jiang, S.-L. Chou, S. X. Dou, H. K. Liu, J. Yang, *ACS Nano* **2016**, *10*, 10524, doi: 10.1021/acsnano.6b06517.
- [28] C. Berg, R. Morasch, M. Graf, H. A. Gasteiger, *J. Electrochem. Soc.* **2023**, *170*, 030534, doi: 10.1149/1945-7111/acc09d.
- [29] Z. Yan, S. Yi, X. Li, J. Jiang, D. Yang, N. Du, *Mater. Today Energy* **2023**, *31*, 101225, doi: 10.1016/j.mtener.2022.101225.
- [30] H. Ren, J. Sun, R. Yu, M. Yang, L. Gu, P. Liu, H. Zhao, D. Kisailus, D. Wang, *Chem. Sci.* **2016**, *7*, 793, doi: 10.1039/C5SC03203B.
- [31] B. Lu, B. Ma, X. Deng, B. Wu, Z. Wu, J. Luo, X. Wang, G. Chen, *Chem. Eng. J.* **2018**, *351*, 269, doi: 10.1016/j.cej.2018.06.109.
- [32] J. Xiang, H. Liu, R. Na, D. Wang, Z. Shan, J. Tian, *Electrochim. Acta* **2020**, *337*, 135841, doi: 10.1016/j.electacta.2020.135841.
- [33] K. Feng, M. Li, H. Park, G. Lui, W. Liu, A. G. Kashkooli, X. Xiao, Z. Chen, *J. Power Sources* **2018**, *399*, 98, doi: 10.1016/j.electacta.2020.135841.
- [34] T. Tang, Z. Sun, X. Bi, X. Shi, W. Wu, X. Ge, C. Tao, Z. Zhang, J. Wang, *Nanotechnology* **2021**, *33*, 025403, doi: 10.1088/1361-6528/ac2d49.
- [35] T. Mu, S. Lou, N. G. Holmes, C. Wang, M. He, B. Shen, X. Lin, P. Zuo, Y. Ma, R. Li, C. Du, J. Wang, G. Yin, X. Sun, *ACS Appl. Mater. Interfaces* **2021**, *13*, 4093, doi: 10.1021/acsmami.0c21455.
- [36] J. C. Meyer, C. Kisielowski, R. Erni, M. Rossell, M. F. Crommie, A. Zettl, *Nano Lett.* **2008**, *8*, 3582, doi: 10.1021/nl801386m.
- [37] H. Shang, Z. Zuo, L. Yu, F. Wang, F. He, Y. Li, *Adv. Mater.* **2018**, *30*, 1801459, doi: 10.1002/adma.201801459.
- [38] Y.-X. Wang, S.-L. Chou, J. H. Kim, H.-K. Liu, S.-X. Dou, *Electrochim. Acta* **2013**, *93*, 213, doi: 10.1002/adma.201801459.
- [39] M. Wagemaker, W. J. H. Borghols, F. M. Mulder, *J. Am. Chem. Soc.* **2007**, *129*, 4323, doi: 10.1021/ja067733p.
- [40] J. Wu, H.-W. Liu, A. Tang, W. Zhang, H.-S. Sheu, J.-F. Lee, Y.-F. Liao, S. Huang, M. Wei, N.-L. Wu, *Nano Energy* **2022**, *102*, 107715, doi: 10.1016/j.nanoen.2022.107715.
- [41] X. Yan, Z. Wang, M. He, Z. Hou, T. Xia, G. Liu, X. Chen, *Energy Technol.* **2015**, *3*, 801, doi: 10.1002/ente.201500039.
- [42] J. Wang, S. Li, Y. Zhao, J. Shi, L. Lv, H. Wang, Z. Zhang, W. Feng, *RSC Adv.* **2018**, *8*, 6660, doi: 10.1039/C7RA12027C.
- [43] Z. Sun, X. Ge, W. Wu, X. Shi, J. Gu, H. Jing, J. Wang, Z. Zhang, Y. Lu, *Electrochim. Acta* **2022**, *428*, 140909, doi: 10.1016/j.electacta.2022.140909.
- [44] X. Bi, T. Tang, X. Shi, X. Ge, W. Wu, Z. Zhang, J. Wang, *Small* **2022**, *18*, 2200796, doi: 10.1002/smll.202200796.
- [45] R. Yu, Y. Pan, Y. Jiang, L. Zhou, D. Zhao, G. Van Tendeloo, J. Wu, L. Mai, *Adv. Mater.* **2023**, *35*, 2306504, doi: 10.1002/adma.202306504.
- [46] P. Díaz-Carrasco, A. Duarte-Cárdenas, A. Kuhn, F. García-Alvarado, *J. Power Sources* **2021**, *515*, 230632, doi: 10.1016/j.jpowsour.2021.230632.
- [47] D. J. Morgan, C.-J. Carbon Res. **2021**, *7*, 51, doi: 10.3390/c7030051.
- [48] D. Lv, D. Wang, N. Wang, H. Liu, S. Zhang, Y. Zhu, K. Song, J. Yang, Y. Qian, *J. Energy Chem.* **2022**, *68*, 104, doi: 10.1016/j.jechem.2021.11.040.
- [49] L.-B. Xiong, J.-L. Li, B. Yang, Y. Yu, *J. Nanomater.* **2012**, *2012*, 831524, doi: 10.1155/2012/831524.
- [50] R. M. N. M. Rathnayake, H. W. M. A. C. Wijayasinghe, H. M. T. G. A. Pitawala, M. Yoshimura, H.-H. Huang, *Appl. Surf. Sci.* **2017**, *393*, 309, doi: 10.1016/j.apsusc.2016.10.008.
- [51] A. J. Cooper, N. R. Wilson, I. A. Kinloch, R. A. W. Dryfe, *Carbon* **2014**, *66*, 340, doi: 10.1016/j.carbon.2013.09.009.
- [52] A. Wollbrink, C. H. Rüscher, K. Volgmann, J. Koch, A. Breuksch, C. Tegenkamp, J. Caro, *J. Membr. Sci.* **2017**, *528*, 316, doi: 10.1016/j.jmemsci.2016.12.067.
- [53] S. Rajasekaran, F. Abild-Pedersen, H. Ogasawara, A. Nilsson, S. Kaya, *Phys. Rev. Lett.* **2013**, *111*, 085503, doi: 10.1103/PhysRevLett.111.085503.
- [54] Y. Wang, D. C. Alsmeyer, R. L. McCreery, *Chem. Mater.* **1990**, *2*, 557, doi: 10.1021/cm00011a018.
- [55] L. Bokobza, J.-L. Bruneel, M. Couzi, *Vib. Spectrosc.* **2014**, *74*, 57, doi: 10.1016/j.vibspec.2014.07.009.
- [56] J.-C. Hsu, P. W. Wang, C.-C. Lee, *Appl. Opt.* **2006**, *45*, 4303, doi: 10.1364/AO.45.004303.
- [57] M. J. Jackman, A. G. Thomas, C. Muryn, *J. Phys. Chem. C* **2015**, *119*, 13682, doi: 10.1021/acs.jpcc.5b02732.
- [58] J. A. Quirk, V. K. Lazarov, K. P. McKenna, *J. Phys. Chem. C* **2020**, *124*, 23637, doi: 10.1021/acs.jpcc.0c06052.
- [59] B. Wen, L.-M. Liu, A. Selloni, *J. Chem. Phys.* **2019**, *151*, 184701, doi: 10.1063/1.5126961.
- [60] M. Hannula, H. Ali-Loyty, K. Lahtonen, E. Sarlin, J. Saari, M. Valden, *Chem. Mater.* **2018**, *30*, 1199, doi: 10.1021/acs.chemmater.7b02938.
- [61] H. Lindström, S. Södergren, A. Solbrand, H. Rensmo, J. Hjelm, A. Hagfeldt, S.-E. Lindquist, *J. Phys. Chem. B* **1997**, *101*, 7717, doi: 10.1021/jp970490q.
- [62] T.-C. Liu, W. G. Pell, B. E. Conway, S. L. Roberson, *J. Electrochem. Soc.* **1998**, *145*, 1882, doi: 10.1149/1.1838571.
- [63] N. A. M. Barakat, Y. T. Sayed, O. M. Irfan, M. M. Abdelyat, *PLoS One* **2023**, *18*, e0282869, doi: 10.1371/journal.pone.0282869.
- [64] Y. Lee, S. Kim, J. H. Lee, K. C. Roh, E. Lim, J. Lee, *RSC Adv.* **2019**, *9*, 37882, doi: 10.1039/C9RA07157A.
- [65] A. T. A. Ahmed, C. Bathula, R. Soni, H.-S. Kim, H. Im, S.-W. Lee, W. K. Kim, S. Gedi, A. N. Kadam, *Chemosphere* **2022**, *289*, 133197, doi: 10.1016/j.chemosphere.2021.
- [66] V. Shrivastav, S. Sundriyal, K.-H. Kim, R. K. Sinha, U. K. Tiwari, A. Deep, *Int. J. Energy Res.* **2020**, *44*, 6269, doi: 10.1002/er.5328.
- [67] R. Tao, T. Wang, J. Fan, H. M. Meyer, A. Y. Borisevich, C.-L. Do-Thanh, S. Dai, *ChemNanoMat* **2022**, *8*, 202200075, doi: 10.1002/cnma.202200075.
- [68] Q. He, Z. Sun, X. Shi, W. Wu, J. Cheng, R. Zhuo, Z. Zhang, J. Wang, *Energy Fuels* **2021**, *35*, 2717, doi: 10.1021/acs.energyfuels.0c03580.

Manuscript received: March 29, 2024
Accepted manuscript online: April 7, 2024
Version of record online: April 25, 2024